**EUROPEAN ORGANIZATION FOR NUCLEAR RESEARCH**
CERN — AB DEPARTMENT

# Cryogenic Tunable Microwave Cavity at 13 GHz for Hyperfine Spectroscopy of Antiprotonic Helium

J. Sakaguchi [1], H. Gilg [2], R.S. Hayano, T. Ishikawa, K. Suzuki [3],
E. Widmann _, H. Yamaguchi [4]
*Department of Physics, University of Tokyo, 7-3-1 Hongo, Tokyo 113-0033, Japan*

F. Caspers, J. Eades [5], M. Hori
*CERN, CH-1211 Geneva 23, Switzerland*

D. Barna, D. Horváth
*KFKI Research Institute For Particle and Nuclear Physics, H-1525 Budapest, Hungary*

B. Juhász
*Institute of Nuclear Research of the Hungarian Academy of Sciences, H-4001, Debrecen, Hungary*

H. A. Torii
*Institute of Physics, University of Tokyo, Komaba, Meguro-ku, Tokyo 153-8902, Japan*

T. Yamazaki
*RIKEN Wako Institute, Wako, Saitama 351-0198, Japan*

## Abstract

For the precise measurement of the hyperfine structure of antiprotonic helium microwave radiation of 12.9 GHz frequency is needed, tunable over ±100 MHz. A cylindrical microwave cavity is used whose front and rear faces are meshed to allow the antiprotons and laser beams to enter. The cavity is embedded in a cryogenic helium gas target. Frequency tuning of _ 300 MHz with Q values of 2700-3000 was achieved using over-coupling and an external triple stub tuner. We also present Monte-Carlo simulations of the stopping distribution of antiprotons in the low-density helium gas using the GEANT4 package with modified energy loss routines.

*Geneva, Switzerland*
*1st February 2005*

## 1  Introduction

Here we report the microwave generation and diagnostics part of an experiment to measure the hyperfine structure of antiprotonic helium which was carried out in 2001 and 2003 at the Antiproton Decelerator (AD) of CERN, Geneva [1,2]. The antiprotonic helium ($\overline{\mathrm{p}}\mathrm{He}^+$) atom is a three-body system which consists of an electron, a helium nucleus and an antiproton ($\overline{\mathrm{p}}$). Since it combines both the properties of an atom and a molecule with one negatively charged nucleus, it is often called an "atomcule". It is the only exotic atom which keeps the antiproton for microsecond-scale periods in its orbit [3–5], thus enabling its study with laser and microwave spectroscopy.

The hyperfine structure of $\overline{\mathrm{p}}\mathrm{He}^+$ is caused by the interaction of the magnetic moments associated with the electron spin $\vec{S}_e$, the antiproton angular momentum $\vec{L}_{\overline{p}}$, and the antiproton spin $\vec{S}_{\overline{p}}$. It results in a quadruplet structure consisting of two widely separated doublets with quantum number $\vec{F} = \vec{L}_{\overline{p}} + \vec{S}_e$ (cf. Fig. 1), where two M1 transitions $\nu_{\mathrm{HF}}^-$ and $\nu_{\mathrm{HF}}^+$ can be excited between states belonging to different doublets by microwave radiation. Depending on the quantum states, the frequency of these transitions is in the range of $10-15$ GHz. Within one quadruplet, the two frequencies differ by $\sim 30 - 200$ MHz. For the experiment we chose to study the $(n, L) = (37, 35)$ state ($n$ denotes the principal quantum number and $L$ the angular momentum quantum number) for which the transition frequencies were predicted to be $\nu_{\mathrm{HF}}^+ =$12.896 GHz and $\nu_{\mathrm{HF}}^- = 12.924$ GHz [6–8], with a difference of 28 MHz. The theoretical accuracy was estimated to be $\sim 5 \times 10^{-5}$ corresponding to 0.6 MHz for $\nu_{\mathrm{HF}}^+$ and $\nu_{\mathrm{HF}}^-$.

* Corresponding Author. Tel. +81-3-5841-4234, Fax +81-3-5841-7642
  *Email address:* widmann@nucl.phys.s.u-tokyo.ac.jp (E. Widmann).
[1] Present address: Department of Electronic Engineering, University of Electro-Communications, Tokyo, Japan
[2] Present address: Filchnerstr. 3, D-89231 Neu-Ulm, Germany
[3] Present address: Physik Department, Technische Universität München, James-Franck-Straße D-85748 Garching, Germany
[4] Present address: Center for Nuclear Study (CNS), University of Tokyo, RIKEN campus, Wako, Saitama 351-0198, Japan
[5] Present address: Department of Physics, University of Tokyo, Japan

The application of tunable microwave radiation is a difficult task because the $\overline{p}He^+$ atoms are formed by stopping antiprotons in a cryogenic helium gas target. Furthermore, two laser pulses are needed in addition, one to create a population asymmetry between the lower and upper doublets before applying the microwave, and the second afterwards to detect the population change caused by the microwave radiation. Numerical calculations showed [9] that an oscillating magnetic field $H_0$ of several Gauss is needed to saturate the M1 transitions. For this we developed a cylindrical microwave cavity whose front and rear faces were meshed to allow the antiprotons, the laser beams, and the cold helium gas to enter. The frequency tuning was achieved by an external triple stub tuner. The cavity together with the microwave generation and diagnostics system is described in the following.

After a general overview of the experimental setup (section 2), we present Monte-Carlo calculations of the stopping distribution of $\overline{p}$ in the helium gas (section 3) which define the required size of the cavity. Then we describe the cavity itself (section 4) including the tuning by a triple stub tuner, the microwave generation and diagnostics (section 5), and discuss the accuracy and absolute calibration of the microwave frequency (section 6).

## 2   Overview, cryostat, and annihilation detection

Our $\overline{p}He^+$ spectroscopy has been performed at the AD (Antiproton Decelerator) [10] at CERN, which provided a pulse of $2-4 \times 10^7$ low-energy antiprotons once per 2 minutes in 2001, and once per 85 seconds in 2003 [11]. We set a cryogenic helium target on one of the extraction beamlines of the AD (see Fig. 2). The $\overline{p}$ beam of kinetic energy $\sim 5.3$ MeV traverses a 50 $\mu$m Upilex (a type of polyimide) window at the end of the AD beam line, a variable degrader, a 1 cm air gap, another 50 $\mu$m Upilex window at the entrance of the cryostat, two 7.5 $\mu$m thick super-insulation foils and a 25 $\mu$m stainless steel window at the entrance of the helium target, and finally stops in the target region filled with cold $^4$He gas (temperature $\sim 6.1$ K and pressures between 130 and 530 mbar). The main body of the cryostat (see Fig. 3) is a commercial product (AS Scientific Products type Standard Orange 50). The inset to hold the cavity was designed and manufactured in the CERN central workshop. The lower part around the cavity is made by electro-erosion of stainless steel 316 LN. It has two windows on opposite sides, a stainless steel one for the antiprotons and a quartz (fused silica) window for the laser beams. The foil of the stainless steel window (thickness 25 $\mu$m) is electron-beam welded between two stainless steel rings, and the rings are electron-beam welded into the structure. After pressurizing it to 12 bar to test safe operation at 10 bar, it is plastically deformed to a concave shape with sagitta of $\sim 3.5$ mm. The cryogenic quartz window is made by Connecteurs Electriques Deutsch, Divi-

sion Verelec Hermetics, by brazing a fused silica disk (Suprasil) into a Kovar cylinder and can stand 12 bar overpressure. The Kovar (an iron-nickel-cobalt alloy) cylinder is electron-beam welded into the inset. A second fused silica window is attached to the outer vacuum vessel of the cryostat, sealed by an O-ring.

After stopping in the helium gas, the $\overline{p}$ form antiprotonic helium atoms, some 3% of which are metastable. Upon the arrival of every $\overline{p}$ bunch (hence $\overline{p}He^+$ production) we receive a trigger signal from the accelerator control, with which a laser pulse is fired from a laser hut about 20 m away. Its wavelength is tuned on the $f^+$ transition from metastable state $(n, L) = (37, 35)$ to a short-lived state $(38, 34)$ (cf. Fig. 1), which amounts to 726.091 nm at a typical target pressure of 250 mbar. We use a commercial dye laser system (Lambda Physik Scanmate 2E) with a Littrow-mounted grating and a Piezo-mounted intra-cavity etalon, and pump it with a Q-switched Nd:YAG laser (Coherent Infinity). Around $\lambda \sim 726.091$ nm a typical bandwidth of 600 MHz was achieved [12,13]. The laser pulse induces a transition from a metastable to a short-lived state, from which the $\overline{p}He^+$ atom is rapidly destroyed by annihilation of the $\overline{p}$ with one of the nucleons. The emitted charged pions are detected in Cherenkov counters that are read out in an analog way [14,15] via a digital storage oscilloscope (DSO). The laser pulse leads to a sharp spike in the analog delayed annihilation time spectrum (ADATS) recorded by the DSO whose area $I(t_1)$ is proportional to the population of the metastable state at the arrival time $t_1$ of the laser pulse [16].

The laser pulse is split into two beams, both counter-propagating with respect to the antiproton beam, one of which goes through a 160 ns delay line. The resulting successive pulses thus have an interval of 160 ns, and enter the helium target through two quartz windows. The first pulse creates a population asymmetry between the $F^+$ and $F^-$ doublet. During the same period we apply microwave radiation from a pulsed Travelling Wave Tube Amplifier (TWTA). The second laser pulse measures the population of the $F^+$ doublet at time $t_2$ after the microwave radiation has been applied. If the microwave radiation is resonant with $\nu_{HF}^+$ or $\nu_{HF}^-$, population is transferred from the $F^-$ doublet to the $F^+$ one, and the intensity $I(t_2)$ of the second laser spike is increased compared to an off-resonance case. In the experiment, we keep the laser frequency constant at $f = f^+$ and measure the ratio $I(t_2)/I(t_1)$ as a function of the microwave frequency $\nu_{MW}$.

To generate the microwave field at the $\overline{p}$ stopping region we insert a stainless steel microwave cavity into the target chamber. The cavity is connected by a cryogenic waveguide to the TWTA outside the cryostat. The excitation of the field inside can be monitored by a transmission signal which originates from a probe antenna attached to the cavity wall opposite to the waveguide. Descriptions of the individual parts will be given in the following sections.

4

# 3 Stopping distribution of antiprotons

In order to excite the metastable $\overline{\text{p}}\text{He}^+$ by a strong enough microwave field, it is necessary to stop them inside a resonating cavity. The typical dimension of a cavity is of the order of the wavelength of the resonant field $\lambda_{\text{MW}} = c/\nu_{\text{MW}}$, which is about 23.2 mm for $\nu_{\text{MW}} = 12.9$ GHz. The stopping distribution of antiprotons should be ideally much smaller than that to avoid a strong variation of the oscillating magnetic field for $\overline{\text{p}}$ stopping at different locations.

The size of the stopping distribution is determined by the momentum ($p = 100$ MeV/$c$) and emittance of the AD beam, and the density of the helium target. Choosing typical target conditions of 6.1 K and 250 mbar ($\rho = 3.5 \times 10^{20}$ cm$^{-3}$), a Monte-Carlo simulation [17] was performed using the GEANT 4 toolkit [18] that claims to accurately calculate the stopping power at low energies. GEANT 4 includes also the Barkas effect [19], i.e. the effect that negative particles show a smaller energy loss than positive ones when their velocity approaches the typical velocity of electrons in the target medium, the Bohr velocity $v_{\text{B}} = \alpha c$. For antiprotons this corresponds to a kinetic energy of $T_{\overline{\text{p}}} = 25$ keV, but deviations from the proton stopping power start already just below $T_{\overline{\text{p}}} \sim 1$ MeV [20]. GEANT 4 only treats the Barkas effect down to kinetic energies of 500 keV, which was found not to be sufficient for our case. We therefore had to modify the energy loss routines to reproduce the stopping power of antiprotons in helium as measured by the OBELIX collaboration [21]. The input parameters used for the simulations are listed in Table 1.

Fig. 4 shows the result of the simulation. For the chosen degrader thickness of 77.5 $\mu$m the large majority of antiprotons stops within the cavity which is described in the next section. Due to the angular scattering, the antiproton stopping distribution perpendicular to the beam direction is increased to $\sim 11$ mm (FWHM). The range straggling and the momentum spread of the $\overline{\text{p}}$ beam lead to a width of the stopping distribution in beam direction of $\sim 4$ mm (FWHM).

The accuracy of the simulation was checked experimentally by adding additional degrader until some of the antiprotons stopped in the entrance window. By observing the intensity of a known laser resonance as a function of the degrader thickness the fraction of the $\overline{\text{p}}$ stopped in the helium gas could be deduced. The result agrees well with the simulations, showing that the range and angular scattering are accurately estimated by the modified GEANT 4 code (cf. Fig. 5).

The dashed horizontal lines in Fig. 4 indicate the waist of the laser beam. Atomcules outside this region will see a reduced laser intensity and will therefore only weakly contribute to the expected signal.

5

# 4   Tunable low-temperature cavity

The largest challenge of the cavity design is that it should allow tuning of the resonance frequency by at least $\pm 100$ MHz, though the resonance frequency of a cavity is generally determined by its geometry. A common solution is to change the cavity size mechanically, or to use a mechanically movable plunger to tune the resonance frequency. But in a cryogenic environment, the implementation of moving parts is quite difficult. Another way is to make a rigid cavity of a fixed center frequency of $\nu_C \sim 12.9$ GHz and high intrinsic ("unloaded") $Q$-value $Q_0 > 1000$ ($Q \equiv \nu_C / \Delta\nu$, where $\Delta\nu$ is the width of the resonance curve), and to over-couple the cavity to the external waveguide. This results in a low "loaded" $Q$-value $Q_L = Q_0 / (1 + \beta)$ ($\beta$ = coupling coefficient). For a large $\beta$ (*i.e.* over-coupling), $Q_L$ becomes much smaller than $Q_0$. Choosing a loaded $Q$-value of $Q_L \approx 100$, frequencies can be generated over a wide range ($\pm \nu_C / Q_L \sim \pm 100$ MHz). The oscillating magnetic field in the cavity is by a factor $\sqrt{Q}$ larger than the exciting field applied in the waveguide. To again increase the $Q$-value of the over-coupled cavity, we attached a triple stub tuner (TST) to the waveguide outside the cryostat and used it to compensate the circuit total $Q$-value. The result is that the resonance frequency can be adjusted over a wide range by changing the TST settings, with an effective $Q$-value $Q_{\text{eff}}$ close to the unloaded $Q_0$ of the cavity.

## 4.1   Design and fabrication

Our cavity had to satisfy several requirements:

*i)* Resonance field pattern.
   For helium target conditions of 6.1 K and 250 mbar the stopped $\bar{\text{p}}$ spread spatially over about 11 mm (FWHM) in the $X$-$Y$ direction (perpendicular to the beam) as shown in the previous section. Out of this distribution the laser beam, which is usually narrower to achieve high enough power density, cuts out a fraction that contributes to the signal. The field distribution is desired to be concentrated in and uniform over the region where the laser is applied. Also it should be uniform in the $Z$ direction (*i.e.* beam direction) so that we do not have to adjust the $\bar{\text{p}}$ stopping range too accurately. In short, the field must have few nodes in the $X$-$Y$ plane and no node in the $Z$ direction at $X = Y = 0$.

*ii)* Cavity size vs. resonance frequency.
   The size of the resonant field, which is approximately given by $\lambda/2 \sim 12$ mm and in particular depends on the resonance mode, should be comparable to the stopping distribution.

To satisfy both conditions we chose a $\mathrm{TM}_{110}$ mode of a cylindrical cavity, with a diameter of 28.3 mm (see field pattern in Fig. 6). The resonance frequencies of $\mathrm{TM}_{nml}$ (or $\mathrm{TE}_{nml}$) modes for a cavity with a radius $a$ and an axial length $d$ are given by $\frac{c}{2\pi}\sqrt{\left(\frac{\mathrm{P}_{nm}}{a}\right)^2 + \left(\frac{l\pi}{d}\right)^2}$ ($\mathrm{P}_{nm}$ stand for the zeros, or points of extremes, of Bessel functions) [22], and for the chosen value $d = 24.6$ mm no other mode competes within 800 MHz (see Table 2).

Fig. 7 shows the oscillating field strength and the stopping distribution over the region that is illuminated by the laser beam of 2.5 mm waist. Along the cavity axis, the field drops slightly towards the center. Around the stopping region, the field strength varies at most by about $\pm 10\%$.

The cavity was made of stainless steel 304 with an outer diameter of 34 mm. Since there is another requirement to allow free entrance of $\overline{\mathrm{p}}$ and laser pulses, both circular faces have 15 mm diameter holes, which are covered by meshes of wire thickness (parallel to the cavity axis) 0.3 mm, wire width (perpendicular to the cavity axis) 60 $\mu$m, and wire-to-wire distance 0.74 mm (see Fig. 8), yielding a transmission of 92%. The meshes were made of stainless steel 304 by electro-erosion and are attached to the cavity by electron-beam welding. A rectangular WR75-band waveguide (frequency range 10–15 GHz) is welded to the cavity with an iris in between. The iris dimension ($\sim 10$ mm $\times$ 9.5 mm) was chosen to achieve over-coupling of the microwave cavity (unloaded $Q_0 \sim 2300$) to the waveguide resulting in a loaded $Q$ of $Q_L \sim 100$ (see next section). Most components inside the cryostat are made of stainless steel to reduce heat load and temperature dependence. The waveguide was equally made of stainless steel, but its inside was covered by an electrolytically deposited, 20 $\mu$m thick copper layer to reduce microwave transmission losses. The connection to the room temperature and the atmospheric pressure is made by an alumina window which has more than 97% microwave transmittance and can stand 10 bar pressure without leakage. Opposite to the waveguide a pick-up antenna is attached to the cavity via a standard SMA adapter screwed into a tapped hole. The cavity pick-up is connected to the outside by a cryogenic coaxial cable (Kama Instrumentation) that also uses an inner conductor made of stainless steel and covered by a thin copper coating.

### 4.2 Triple stub tuner

Tuning of the resonance frequency is realized with a triple stub tuner (TST). The triple stub tuner has three side-pockets terminated by choke structures (cf. Fig. 9), and the choke positions of the tuners are variable from 0 mm (at the waveguide wall) to 25 mm with 0.25 $\mu$m stepping using actuators (Sigma Koki DMY25) controlled either manually or remotely via GPIB. It is inserted in the outside part of the waveguide, and under proper choice of the choke

positions the resonance profile of the whole circuit can be adjusted to have a narrow resonance ($Q = 2700$–$3000$) around an arbitrary frequency within the cavity tuning range [6]. The TST creates a resonating structure which includes the cavity, waveguide, and the TST itself. The total structure has a narrow resonance profile.

A three-dimensional field simulation including the cavity and triple stub tuner was performed by Nihon Koshuha Co, Ltd., using the High Frequency Structure Simulation (HFSS) code to choose the correct iris diameter and to calculate the magnetic field distribution inside the cavity. The cavity dimensions were always diameter 28.3 mm and length 24.6 mm. In Fig. 6 the result of a simulation with an iris size of 9 mm $\times$ 9.525 mm and thickness of 1 mm is shown. The simulation gave an effective $Q$-value of $Q_{\text{eff}} = 1502$, and a maximum oscillating magnetic field strength of $H_0 \sim 60$ Gauss for an input microwave power of 2 kW. This is in very good agreement with a calculation using the analytical formula for a $TM_{110}$ mode [22] for these parameters. The loaded $Q$-value of cavity plus waveguide for this configuration was still rather high ($Q_L \sim 677$), so that the final cavity had a slightly larger iris to create a larger over-coupling. The parameters of the final cavity are given in Table 3. It satisfies the requirement of a loaded $Q$-factor of about $Q_L \sim 100$ to allow a large tuning range.

Actual examples of the tuned resonance spectra (measured in an diagnostic mode explained in the next section) are shown in Fig. 10. Two different settings of the choke positions give totally different resonance profiles for the reflection from the cavity and for the transmission from the probe antenna. For the case of Fig. 10(b) a resonance condition is attained at a probe microwave frequency $\nu_M = 12.896$ GHz which is just around the M1 transition frequency $\nu_{\text{HF}}^+$ (see Fig. 1), and for the case of Fig. 10(a) it is also attained even at 300 MHz lower frequency.

## 5 Microwave diagnostics and generation

The microwave radiation is generated by a vector network analyzer (VNA: Anritsu 37225B) used in continuous wave (CW) mode as a synthesizer, whose output is pulse-amplified by a Travelling Wave Tube Amplifier (TWTA: Thorn Microwave Device PTC6358). The microwave system is operated in two different modes. One is a diagnostic mode in which we measure the microwave resonance profile of the cavity system, and another is the operation mode to

---

[6] The tuning (or impedance matching) becomes difficult as the reflection from the cavity goes close to 1, so the range of the frequency tuning is determined by the width of the resonance profile without TST, *i. e.* the loaded $Q$-value.

feed the microwave field into the cavity. The switching between the two modes is done with a remote-controlled motorized waveguide switch (Nihon Koshuha WGSA-1285). Between two antiproton pulses from the AD, a sequence — *i)* setting TST for new central frequency $\nu_C$, *ii)* measure cavity parameters to verify $\nu_C$ and $Q_{\mathrm{eff}}$, *iii)* setting the frequency of the microwave source and waiting for the $\overline{\mathrm{p}}$ to arrive — is performed by computer control.

## 5.1 Diagnostic mode

The upper part of Fig. 11 illustrates the scheme of the diagnostic mode. This mode is used before the arrival of a $\overline{\mathrm{p}}$ pulse, after the frequency has been set by the TST, to see whether the correct resonance condition was obtained. The microwave signal from port 1 of the VNA is divided by a directional coupler (ARRA 6-9194-10) into two paths, of which one, the "side branch", is attenuated by 10 dB, the other being followed by the main signal.

The main signal travels a Suhner Sucoflex 104 cable with SMA connectors and goes into the motorized waveguide switch through a SMA-to-waveguide transition (PARZICH LD75CA-F). The high-powered fields from the TWTA travel between the waveguide switch and the cavity through a rectangular WR-75 band waveguide like the one inside the cryostat. In the diagnostic mode the signal travels through the waveguide to the microwave cavity, where a part of it is reflected back to the VNA port 1 and another part goes through the pickup antenna and the cryogenic coaxial cable to the VNA port 2 (see Fig. 11). A microwave limiter (Hewlett Packard 11693A) is inserted before the VNA to protect port 2 from high-power radiation. The coupling of the pick-up antenna was adjusted to typically $-32$ dB. The vector network analyzer is calibrated at the calibration planes shown in the figure, and measures the reflection $S_{11}$ (at the plane) and transmission $S_{21}$ parameter (between the planes) as a function of the frequency as shown in Fig. 10. The S-parameters $S_{ij}$ are essentially the complex ratio of the signal (amplitude and phase) measured at port $i$ and $j$ of the VNA. We could alter the resonance frequency by the TST maintaining a very small ($\leq -40$ dB) reflection rate over a wide frequency range.

The microwave signal in the side branch is amplified by a low-noise microwave amplifier (MITEQ AFS4-08001800-35-LN) to $\sim 10$ dBm (dB relative to 1 mW, see lower part of Fig. 11). The amplified signal is split by a 90-degree hybrid coupler (ARRA 6-9164-90X) into two. One is used to feed the Travelling Wave Tube Amplifier after being attenuated by a voltage-controlled attenuator (VCA: G.T.Microwave, Inc. A6L-78N-7). With 0 V control voltage the attenuator degrades the signal only by its insertion loss, and with 1 V increase of the voltage the output signal gets degraded by $\sim 8$ dB. This way the output power of the TWTA which has a constant amplification of 78

9

dB can be adjusted by remote control. The power of the microwave signal at the input port of the TWTA was calibrated with CW signals by a microwave power meter and the result is shown in Fig. 12. In the diagnostic mode we keep the control voltage to be 10 V, thus no microwave goes into the TWTA.

## 5.2  Operation mode

As soon as the VNA finishes diagnosis, the system changes into the operation mode by turning the motorized waveguide switch and waits for the trigger signal from AD control. In this mode the VNA acts as a narrow-band microwave source with a YIG synthesizer. The YIG oscillator is phase-locked to a quartz oscillator, and the signal is stabilized to the level that the phase noise of the CW signal is 60 dBc/Hz (dBc = dB below carrier level) at 10 kHz offset and 20 GHz center frequency. Harmonic (and non-harmonic) spurious signals are less than 35 dBc, which will be further degraded by a harmonic filter. The microwave frequency is set to the resonance frequency of the circuit acquired in the diagnostic mode. The power of the TWTA input is controllable from $\sim -50$ dBm to $\sim -15$ dBm by the voltage controlled variable attenuator described above. When the arrival of $\overline{\mathrm{p}}$ (hence the production of $\overline{\mathrm{p}}\mathrm{He}^+$) is announced by the AD trigger, a programmable pulse generator (LeCroy 9210) generates a gate signal of 20 $\mu$s length to the TWTA, and the TWTA amplifies its input microwave signal and feeds it into the cavity according to this gate signal. Between the TWTA and the cavity a microwave isolator and a high power harmonic filter are placed. The isolator (RYT Industries 401328) has a forward transmission of 90% and backward transmission of $-50$ dB and prevents reflected waves damaging the TWTA. The filter attenuates harmonic signals with $25 \sim 26.8$ GHz frequency by 40 dB. The specification of the TWTA gain at the microwave frequency $\nu_{\mathrm{M}} \sim 12.9$ GHz is 78 dB. Since it is designed for a higher duty-cycle than used in our experiment, warming up operation (with $\sim 10$ Hz trigger rate) is required before (and after) each high-power shot.

After we send the microwave pulse, we monitor the amplified field, by down conversion of the microwave-frequency signals to DC signals using I/Q mixers (MITEQ IR0618LC2Q). An I/Q mixer is a circuit of nonlinear devices which mixes an RF input signal with a reference RF signal (called Local Oscillator, LO), and outputs DC signals proportional to the in-phase (I) and quadrature (Q) component of the input signal against the LO signal. We use two mixers, one to monitor a sample output of the TWTA (which is 50 dB weaker than the main output) and one for the transmission signal from the pickup antenna on the cavity. In our circuit the LO signal is provided by splitting the signal coming from the VNA and amplifying it by a microwave amplifier (MITEQ AMF-3F-100150-40-15P). The other inputs of the mixers receive the signals

from the TWTA sample output port and the pickup, both degraded slightly by attenuators to adjust the proper maximum input power to the mixers. When the input signal oscillates with the same frequency $\omega$ as that of the LO signal (but with a different phase $\phi$) as $V_{\mathrm{LO}}(t) = V_{\mathrm{LO}}\cos(\omega t)$ and $V_{\mathrm{in}}(t) = V_{\mathrm{in}}\cos(\omega t + \phi)$, I and Q outputs of the mixer are obtained from multiplication of the two input voltages as $V_{\mathrm{I}} \propto V_{\mathrm{LO}}V_{\mathrm{in}}\cos(\phi)$ and $V_{\mathrm{Q}} \propto V_{\mathrm{LO}}V_{\mathrm{in}}\sin(\phi)$ respectively. These DC signals are recorded by a digital oscilloscope (DSO-MW: Tektronix TDS420A), and we can calculate the output signal power $P_{\mathrm{I}/Q}$ as

$$P_{\mathrm{I}/Q} = (V_{\mathrm{I}}^2 + V_{\mathrm{Q}}^2)/Z_c, \tag{1}$$

($Z_c = 50\ \Omega$: impedance of the transmission line), and the signal phase $\phi_{\mathrm{I}/Q}$ as

$$\phi_{\mathrm{I}/Q} \propto \tan^{-1}(V_{\mathrm{Q}}/V_{\mathrm{I}}). \tag{2}$$

A typical example of amplitude and phase of the signals measured by the $I/Q$-mixers is shown in Fig. 13. We performed a calibration of input/output powers of the mixers using the variable attenuator, and the results are plotted in Fig. 14. We observe a linear correlation between the input powers and the output powers.

The output microwave power $P_{\mathrm{M}}$ of the TWTA can be estimated from the monitored signals. For the case of Fig. 13, the power of the TWTA sample-port signal recorded by the oscilloscope was 1.5 $\mu$W$\sim -28$ dBm when we send a typical input power of $\sim -30$ dBm to the TWTA. Considering the mixer insertion loss (6 dB) and the attenuation (50 dBc of the sample port of the TWTA and 16 dB between sample port and mixer), we estimate that $P_{\mathrm{M}}$ was $\sim 44$ dBm (= 25 W) and the TWTA gain was $\sim 74$ dB, which is close to the specified value. For microwave power measurements it is difficult to avoid a few dB inaccuracies which come from losses in the cables, connectors, feed throughs, and so on.

The $P_{\mathrm{M}} \sim 44$ dBm microwave field goes through the cavity to the pickup port, with typically $\sim -32$ dB transmission rate (when the resonance condition is achieved by TST) as shown in Fig. 10. During some of the measurements we used DC amplifiers with voltage controlled gain to amplify the output signals of the I/Q-mixers. As we see in Fig. 15, the microwave power estimated from the sample-port signal and that from the pickup signal agree well within $\sim \pm 2$ dB.

The $S_{11}$ and $S_{21}$ signals from the VNA as well as the I/Q mixer outputs from the DSO-MW are recorded for each shot, so that the actual frequency and power can be evaluated off-line for any measurement point.

# 6 Accuracy of the microwave frequency

The experiment consists of a search for transitions induced by microwave pulses applied during the time interval of $\Delta t = 160$ ns between pairs of laser pulses, resulting in a width of the resonance lines given by the Fourier limit of $\Delta \nu \sim 1/\Delta t \sim 6$ MHz. The relative value is one order of magnitude worse than the errors of the theoretical calculations of $5 \times 10^{-5}$, but the centroid of the resonance lines can be determined with higher accuracy. For the current experiment the knowledge of the absolute frequency of the VNA output to about $10^{-6}$ was therefore sufficient. The VNA is equipped with an oven-controlled quartz oscillator with an resolution of 1 Hz and a specified aging of $< 10^{-9}$/day. In the first run in 2001, the absolute frequency was calibrated once using a microwave frequency counter (Fluke PM6681) which itself was stabilized by a 10 MHz reference signal from a GPS-controlled HP58503B time and frequency receiver available at CERN. Via the atomic clocks on the GPS satellites, this oscillator inside the HP58503B is stabilized to the atomic clocks at NIST, Boulder, Colorado, with an accuracy of better than $10^{-12}$ over 1 day [23]. Microwave signals of 100 MHz and 200 MHz from the VNA were measured with $\sim 10^{-10}$ precision, and an offset of the frequency of about $(0.8 \pm 0.1)$ kHz per 100 MHz was found. Since the output frequencies of the VNA are derived from a single quartz oscillator, we had to apply a relative correction of $(8 \pm 1) \times 10^{-6}$ to the nominal frequencies. The error of $1 \times 10^{-6}$ corresponds to an absolute error of $\sim 13$ kHz in the microwave frequency.

In 2003, we made use of the possibility to stabilize the VNA itself with the 10 MHz signal from a GPS-controlled oscillator. To verify the accuracy we used an independent second HP58503B oscillator to stabilize a HP5342A 18-GHz frequency counter and directly measured the output frequency of the VNA in off-line calibration runs. Over a period of several days, we observed a fluctuation of the microwave counter reading of less than $\pm 5$ Hz from the VNA setting of 12.908 GHz at an averaging time of 1 second, which corresponds to 1 Hz frequency resolution of the HP5342A counter. We conclude that in this case the frequency output of the VNA had an accuracy of about $10^{-9}$.

# 7 Summary

We have described a cryogenic microwave cavity at 12.9 GHz which was successfully used in the spectroscopy of the hyperfine structure of antiprotonic helium. By over-coupling the cavity to the waveguide supplying the microwave radiation and using a triple stub tuner located outside the cryostat, the resonance frequency of the whole system could be scanned over a range of several 100 MHz while keeping Q-factors of $\sim 2700 - 3000$. To determine the size of

the stopping distribution of antiprotons in the low-temperature helium gas we performed Monte-Carlo simulations using the GEANT4 code with modified energy-loss routines. A good agreement was observed between the simulations and measurements of the stopping efficiency of antiprotons inside the cavity.

**Acknowledgements**

# References

[1] E. Widmann, J. Eades, T. Ishikawa, J. Sakaguchi, T. Tasaki, H. Yamaguchi, R.S. Hayano, M. Hori, H. A. Torii, B. Juhász, D. Horváth, and T. Yamazaki, Phys. Rev. Lett. 89 (2002) 243402.

[2] J. Sakaguchi, J. Eades, R. S. Hayano, M. Hori, D. Horváth, T. Ishikawa, B. Juhász, H.A. Torii, E. Widmann, H. Yamaguchi and T. Yamazaki, Nucl. Inst. Meth. B 214 (2004) 89.

[3] M. Iwasaki, S.N. Nakamura, K. Shigaki, Y. Shimizu, H. Tamura, T. Ishikawa, R.S. Hayano, E. Takada, E. Widmann, H. Outa, M. Aoki, P. Kitching and T. Yamazaki, Phys. Rev. Lett. 67 (1991) 1246.

[4] T. Yamazaki, E. Widmann, R.S. Hayano, M. Iwasaki, S.N. Nakamura, K. Shigaki, F.J. Hartmann, H. Daniel, T. von Egidy, P. Hofmann, Y.-S. Kim and J. Eades, Nature 361 (1993) 238.

[5] T. Yamazaki, N. Morita, R. S. Hayano, E. Widmann and J. Eades, Phys. Rep. 366 (2002) 183.

[6] D. Bakalov and V. Korobov, Phys. Rev. A 57 (1998) 1662.

[7] V. Korobov and D. Bakalov, J. Phys. B: At. Mol. Opt. Phys. 34, (2001) L519.

[8] Y. Kino, N. Yamanaka, M. Kamimura and H. Kudo, Hyp. Int. 146-147 (2003) 331.

[9] J. Sakaguchi, Ph. D. thesis, University of Tokyo (2003).

[10] S. Baird *et al.*, Nucl. Phys. B 56 A (1997) 349.

[11] P. Belochitskii, T. Eriksson, and S. Maury, Nucl. Instr. Meth. Phys. Res. B 214 (2004) 176.

[12] M. Hori, J. Eades, R.S. Hayano, T. Ishikawa, J. Sakaguchi, E. Widmann, H. Yamaguchi, H.A. Torii, B. Juhász, D. Horváth, and T. Yamazaki, Phys. Rev. Lett. 87 (2001) 093401.

[13] M. Hori, R.S. Hayano, E. Widmann, and H.A. Torii, Opt. Lett. 28 (2003) 2479.

[14] A. Niestroj, F. J. Hartmann, H. Daniel, B. Ketzer, T. von Egidy, F. E. Maas, R. S. Hayano, T. Ishikawa, H. Tamura, H. A. Torii, N. Morita, T. Yamazaki, I. Sugai, K. Nakayoshi, D. Horváth, J. Eades, and E. Widmann, Nucl. Instr. Meth. Phys. Res. A 373 (1996) 411.

[15] M. Hori, K. Yamashita, R.S. Hayano and T. Yamazaki, Nucl. Inst. Meth. A 496 (2003) 102.

[16] N. Morita, K. Ohtsuki and T. Yamazaki, Nucl. Instrum. Methods A 330 (1993) 439.

[17] B. Juhász, M. Sc. thesis, University of Debrecen (2000).

[18] S. Agostinello *et al.*, Nucl. Instr. Meth. Phys. Res. A 509 (2003) 250.

[19] W.H. Barkas, W. Birnbaum, F.M. Smith, Phys. Rev. 101 (1956) 778.

[20] S.P. Møller, E. Uggerhøj, H. Bluhme, H. Knudsen, U. Mikkelsen, R. Paludan, and E. Morenzoni, Phys. Rev. A 56 (1997) 2930.

[21] M. Agnello et al., Phys. Rev. Lett. 74 (1995) 371.

[22] R.E. Collin, Foundations for microwave engineering (second edition), McGraw-Hill, 1992.

[23] M.A. Lombardi *et al.*, Time and frequency measurements using the global positioning system, Cal Lab Int. Jour. of Metrology, July-September 2001, pp. 26–33, *available from http://www.nist.gov.*
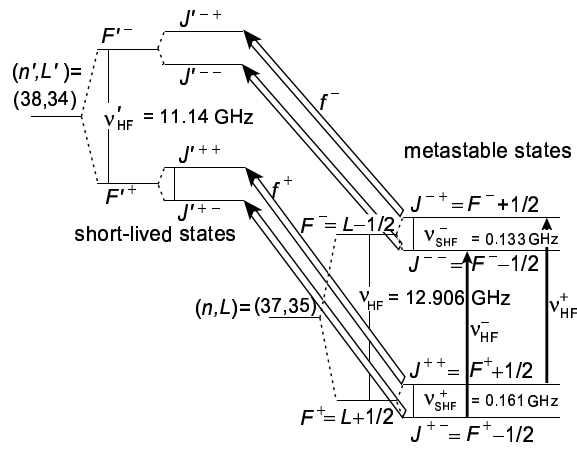
Fig. 1. Level diagrams of two states $(n, L) = (37, 35)$ and $(38, 34)$ and possible laser transitions $(f^+, f^-)$ between them (double-lined arrows). The sub-states are classified by the combined angular momenta $\vec{F} \equiv \vec{L_{\bar{p}}} + \vec{S_e}$ and $\vec{J} \equiv \vec{F} + \vec{S_{\bar{p}}}$. The arrows within the (37,35) quadruplet denote the measured M1 transitions $\nu_{HF}^+$ and $\nu_{HF}^-$.
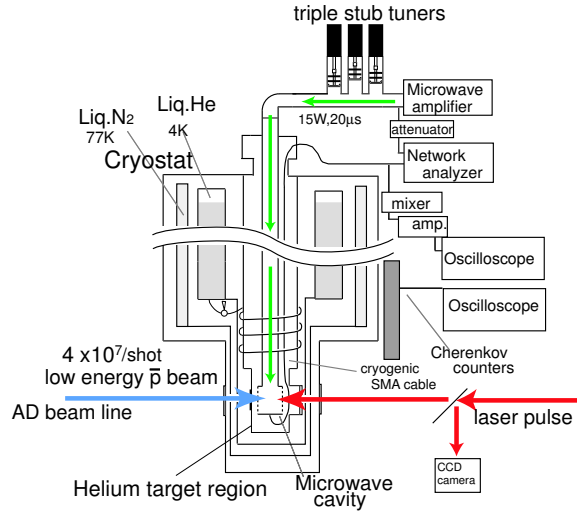


Fig. 2. Schematic drawing of the experimental setup around the target area.

16
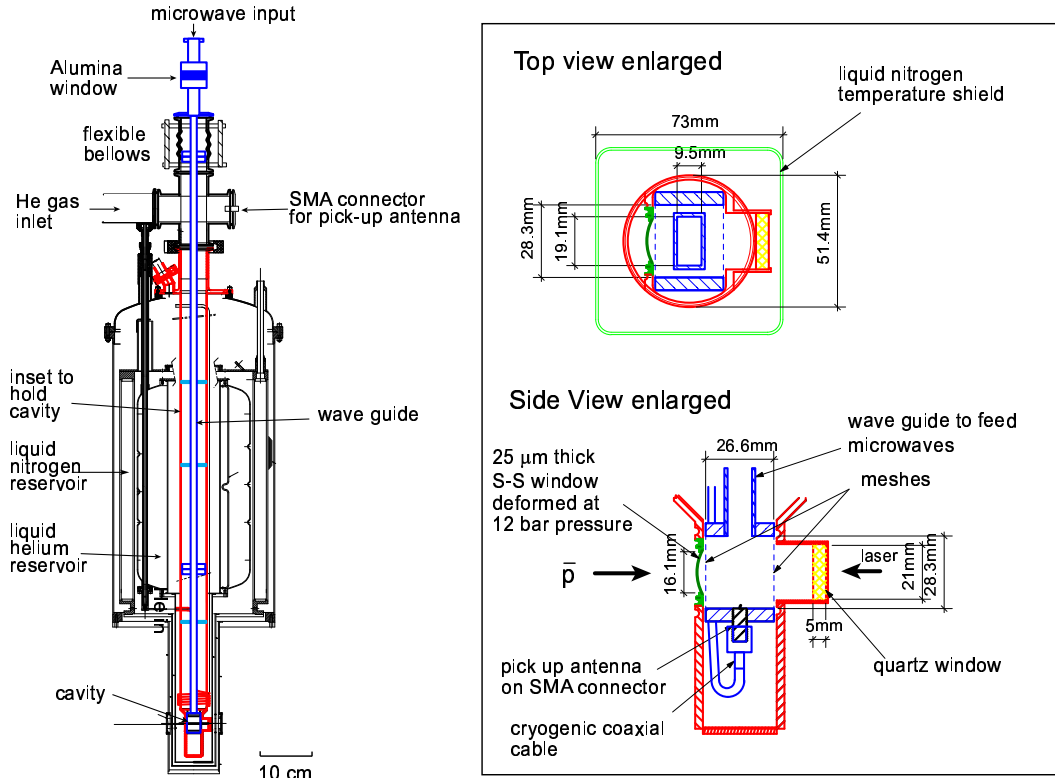
Fig. 3. Left: Detailed drawing of the cryostat with the inset to hold the cavity and with the waveguide. Right: enlarged top and side view of the cavity region.
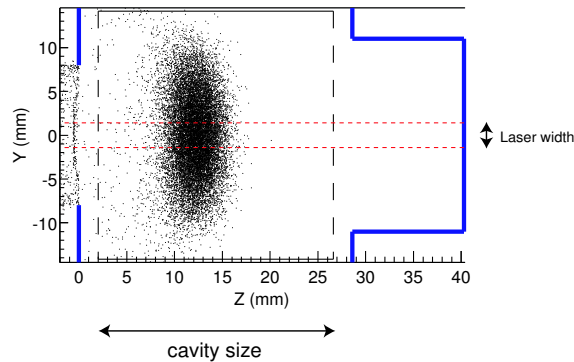


Fig. 4. Stopping distribution of $\overline{\text{p}}$ (top view). The antiprotons enter from left, the laser beam from right. The inner rectangle with two dashed vertical sides representing the meshes signifies the inner walls of the cavity, while the outer thick lines show the walls of the gas chamber. The cavity is placed with the cylinder axis parallel to the $Z$ direction. The dashed horizontal lines indicate the width of the laser beam. The annihilation of a part of the antiprotons in the outward bent entrance window can be seen on the left side of the figure.

17
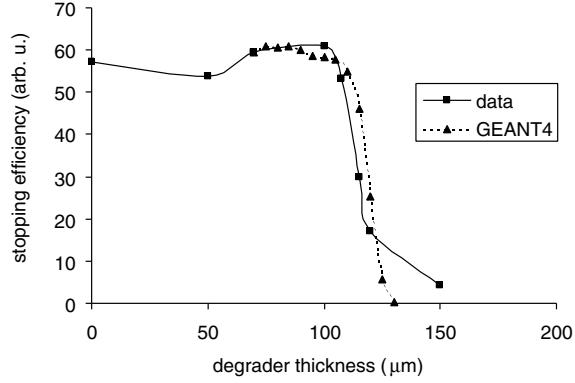
Fig. 5. Comparison of measured and calculated range curve obtained by varying the thickness of the last degrader before the entrance window of the cryostat. The lines are guides to the eye.
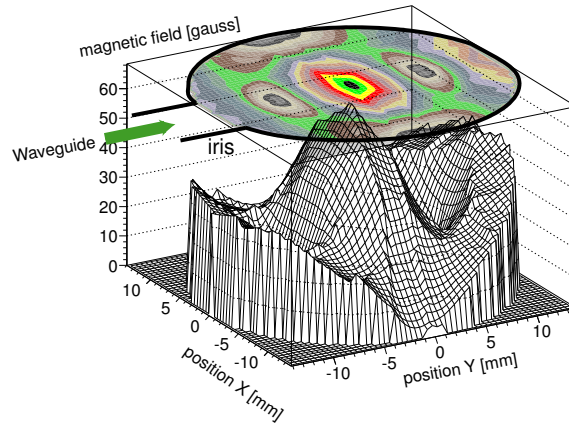


Fig. 6. The $TM_{110}$ mode magnetic field inside the cylindrical microwave cavity, simulated by the High Frequency Structure Simulation (HFSS) code of Ansoft. The dimensions of the cavity and the waveguide are the finally chosen ones. The TST creates a total loaded $Q \sim 1500$. The input microwave power is assumed to be 2 kW. The magnetic field in the $Z = 0$ plane (center of the cavity) is plotted. The waveguide is attached to the $-Y$ direction.

18
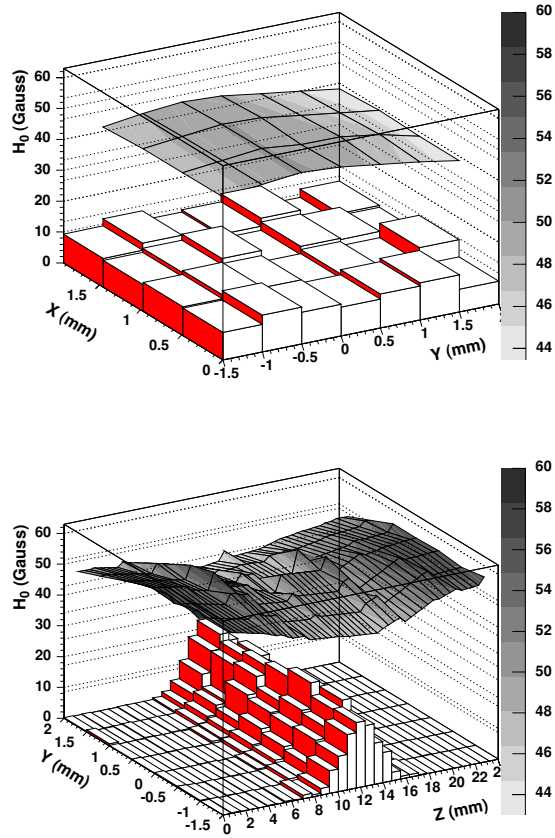
Fig. 7. Upper: Oscillating magnetic field strength $H_0$ (grey-shaded surface) and $\overline{p}$ stopping distribution (Lego plot) over the region covered by the 2.5 mm wide laser beam for the plane perpendicular to the laser beam and the cavity axis. The grey-scale palette gives the magnetic field strength in Gauss. Lower: equivalent distribution for a 2.5 mm wide region along the laser beam and cavity axis.
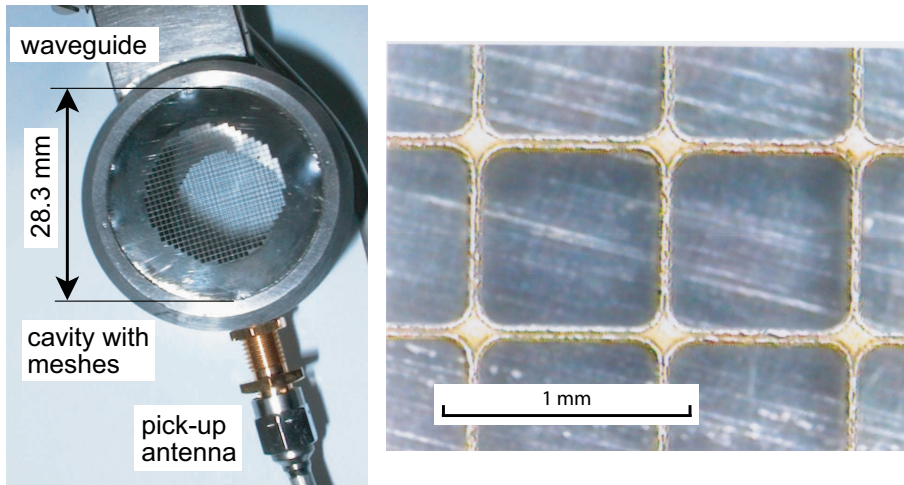


Fig. 8. Left: Photograph of our cylindrical cavity and the connector of the pickup antenna. Right: Photo of a mesh taken through a microscope.
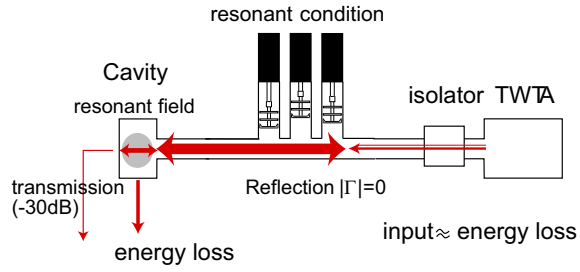
Fig. 9. Schematic drawing of the triple stub tuner inserted between the cavity and the TWTA. The arrows symbolize the microwave radiation, and their thickness reflects the different power levels in the structure.
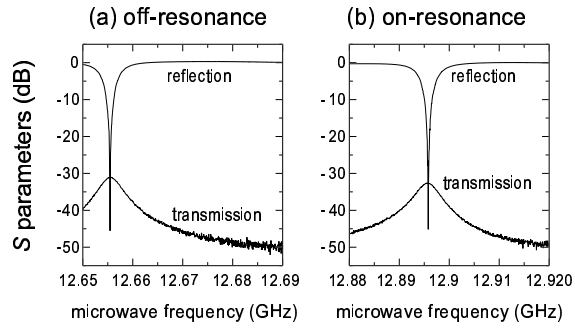


Fig. 10. The resonance profiles of our cavity system measured by the vector network analyzer, with two different stub tuner settings. Reflection stands for the $S_{11}$ S-parameter, transmission for $S_{21}$ (cf. section 5).
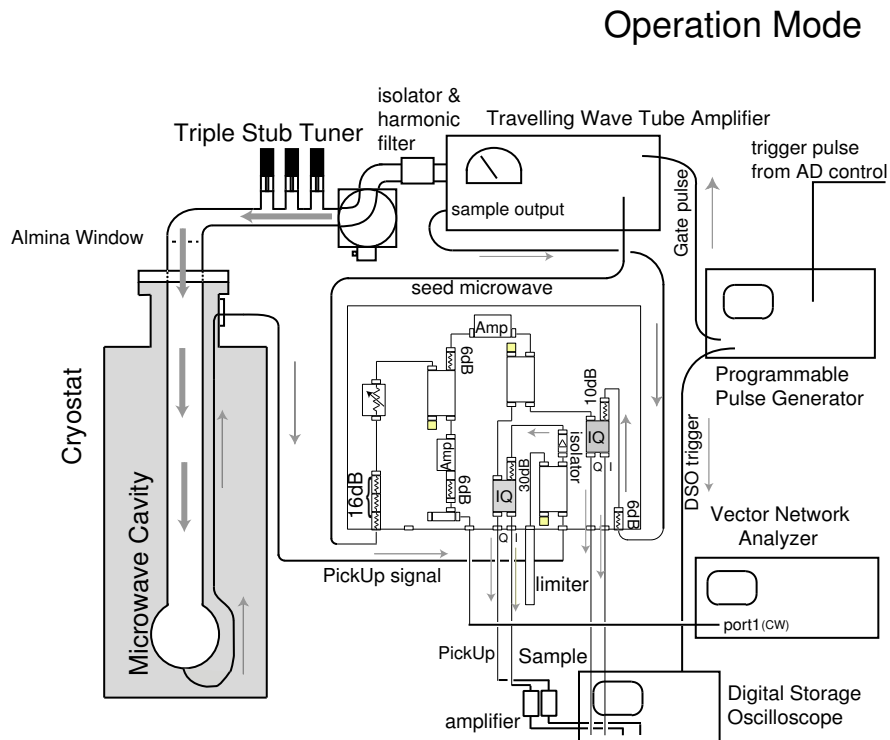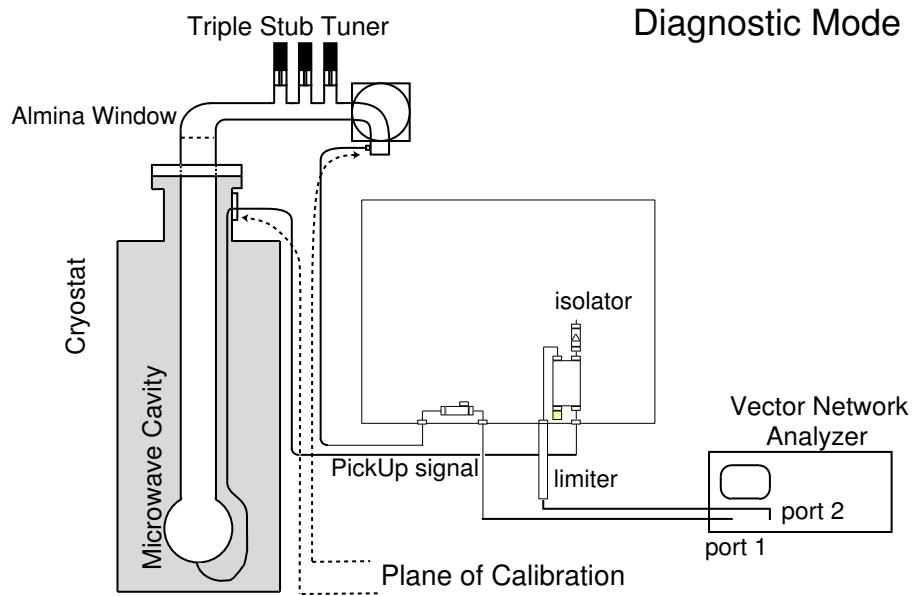
Fig. 11. Two modes of the operation of our microwave circuit. Some inessential parts are omitted.
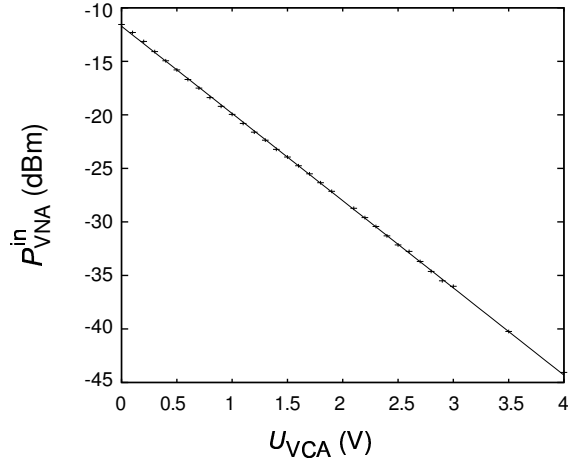
Fig. 12. The input microwave power for the TWTA, $P_{\mathrm{VNA}}^{\mathrm{in}}$, as a function of the voltage $U_{\mathrm{VCA}}$ of the voltage controlled attenuator. Within this range the TWTA input power is controlled linearly by the attenuator voltage. The input level for zero control voltage is adjusted a little bit higher than $-15$ dBm, the input level corresponding to the output saturation level of the TWTA.
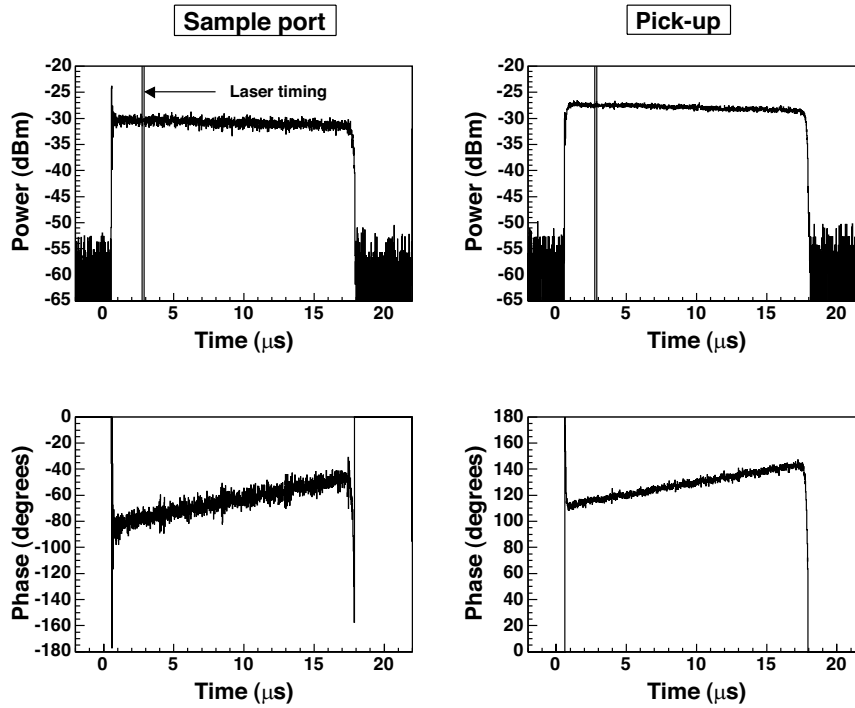


Fig. 13. Typical amplitude and phase signals of one microwave pulse as calculated from the $I$ and $Q$ signals recorded by the digital oscilloscope. The input microwave power to the TWTA was about $-30$ dBm.
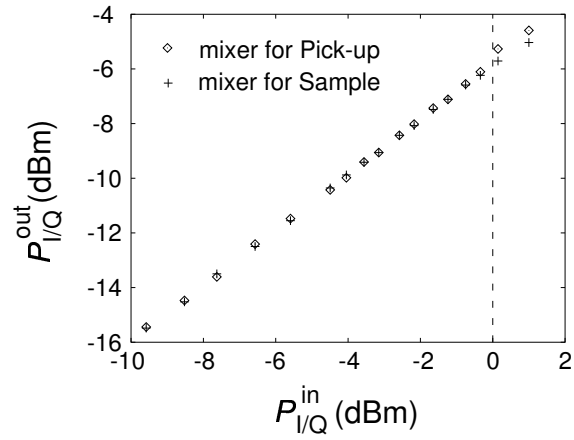
Fig. 14. Relation of the input signal power $P_{I/Q}^{in}$ and the output signal power $P_{I/Q}^{out}$ of the I/Q mixers.
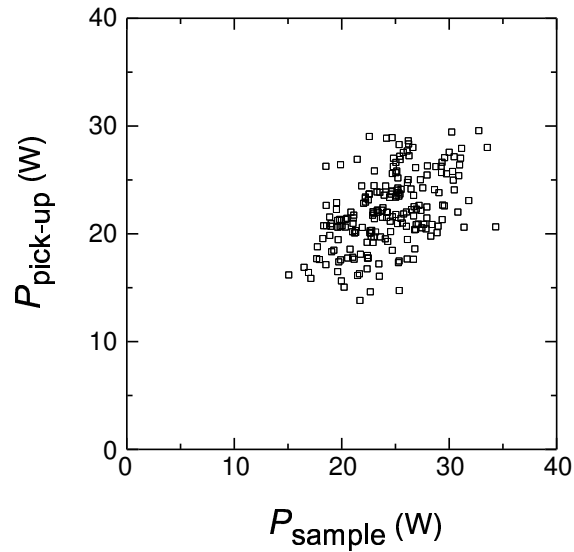


Fig. 15. Relation of the microwave power estimated from the sample-port signal ($P_{sample}$) and the pickup-signal ($P_{pick-up}$) using I/Q mixers.

23

Table 1

Parameters for the calculation of the stopping distribution. Upilex is a foil with the same chemical composition as Kapton, but slightly larger density.

| momentum | 100 MeV/$c$ | momentum spread | $2 \times 10^{-3}$ |
|---|---|---|---|
| beam parameters | horizontal | vertical | |
| divergence [mrad] (95%) | 28.9 | 6.7 | |
| diameter [mm] (FWHM) | 4 | 8 | |
| | material | thickness | |
| beam profile monitor | | | |
| inside vacuum chamber | Upilex | 5 $\mu$m | |
| vacuum gap | – | 3 cm | |
| beam pipe window | Upilex | 50 $\mu$m | |
| air gap | air | 1 cm | |
| degrader | Upilex | 77.5 $\mu$m | |
| cryostat vacuum window | Upilex | 50 $\mu$m | |
| vacuum gap | – | 1 cm | |
| thermal shield | aluminized mylar | 7.5 $\mu$m | |
| vacuum gap | – | 0.7 cm | |
| thermal shield | aluminized mylar | 7.5 $\mu$m | |
| vacuum gap | – | 2 cm | |
| helium chamber window | stainless steel | 25 $\mu$m | |

Table 2

Resonance frequencies of $TM_{nml}$ modes and $TE_{nml}$ modes for a cylindrical cavity, calculated for specified dimensions of $a = 14.15$ mm and $d = 24.6$ mm.

| $n$ | $m$ | $l$ | $\nu$ (GHz) | | $n$ | $m$ | $l$ | $\nu$ (GHz) |
|---|---|---|---|---|---|---|---|---|
| 0 | 1 | 0 | 8.10 | | 1 | 1 | 1 | 8.69 |
| 0 | 1 | 1 | 10.1 | | 2 | 1 | 1 | 12.0 |
| 1 | 1 | 0 | 12.9 | | 1 | 1 | 2 | 13.7 |
| 1 | 1 | 1 | 14.3 | | 0 | 1 | 1 | 14.3 |
| 0 | 1 | 2 | 14.6 | | 2 | 1 | 2 | 15.9 |
| 2 | 1 | 0 | 17.3 | | 1 | 2 | 1 | 18.0 |
| 0 | 2 | 0 | 18.6 | | 2 | 2 | 1 | 23.4 |
| 1 | 2 | 0 | 23.6 | | | | | |

Table 3

Parameters of the cylindrical microwave cavity with attached waveguide, as measured with a vector network analyzer.

| | |
|---|---|
| diameter | 28.3 mm |
| length | 24.6 mm |
| iris | 10.0 mm $\times$ 9.5 mm, thickness 1 mm |
| central frequency | 12.8815 GHz |
| coupling coefficient | 16.023 |
| $Q_L$ | 132.7 |
| $Q_0$ | 2259.0 |